Icarus **137**, 122–139 (1999)
Article ID icar.1998.6031, available online at http://www.idealibrary.com on IDEAL®

Asteroid 4179 Toutatis: 1996 Radar Observations

Steven J. Ostro

Jet Propulsion Laboratory, California Institute of Technology, Pasadena, California 91109-8099
E-mail: ostro@echo.jpl.nasa.gov

R. Scott Hudson

School of Electrical Engineering and Computer Science, Washington State University, Pullman, Washington 99164-2752

and

Keith D. Rosema, Jon D. Giorgini, Raymond F. Jurgens, Donald K. Yeomans, Paul W. Chodas, Ron Winkler, Randy Rose, Dennis Choate, Reginald A. Cormier, Dan Kelley, Ron Littlefair, Lance A. M. Benner, Michael L. Thomas, and Martin A. Slade

Jet Propulsion Laboratory, California Institute of Technology, Pasadena, California 91109-8099

Received May 27, 1998; revised September 29, 1998

We report initial results of daily delay/Doppler observations of Toutatis with the Goldstone 8510-MHz (3.5-cm) radar during Nov. 25–Dec. 3, 1996. Using the physical model of Toutatis derived from 1992 radar observations (Hudson and Ostro 1995, *Science* **270, 84–86) to analyze the new data, we obtain refined estimates of the asteroid's orbit, spin state, and surface properties. The asteroid's centimeter-to-decameter surface characteristics are strikingly uniform. The disc-integrated circular polarization (SC/OC) ratio μ_C averages 0.29 ± 0.01 and is independent of rotational orientation at the several percent level. Dual-polarization images reveal a slight drop in μ_C at echo leading edges, which we interpret as the signature of a smooth surface component. The OC radar albedo averages 0.24 ± 0.03; it depends on rotational orientation, as expected from the asteroid's angular scattering behavior (limb-darkening slightly more than Lambertian). The OC albedo of a sphere with Toutatis' radar properties would be 0.21, or three times the lunar value. The radar properties and available nonradar constraints are consistent with Toutatis' surface having a smooth component that is at least 1/3 covered by rocks at least as large as the wavelength. If this S-class asteroid is mineralogically similar to stony–iron meteorites, then the smooth surface component probably is regolith whose porosity resembles that of lunar soil. If the mineralogy is ordinary chondritic, then the smooth surface component is probably solid with not much more than a centimeter of overlying regolith. We report delay-Doppler astrometry referenced to the asteroid's center of mass (COM) for each day of our experiment. An orbit solution that incorporates those measurements as well as the radar astrometry reported by Ostro** *et al.* **(1995,** *Science* **270, 80–83) and 588 optical astrometric observations from 1988 through March 1997 has weighted rms residuals of 0.98 arcs, 0.10 Hz (1.8 mm s^{-1} in radial velocity), and 0.49 μs in time delay (73 m in range). Integration of that orbit into the past and future shows that Toutatis' pattern of close approaches to Venus, Earth, and Mars is highly asymmetric about the current epoch. The probability of the orbit intersecting Earth is zero for at least the next six centuries. Toutatis will make its closest planetary approach since at least 1353 and until at least 2562 on Sep. 29, 2004, when the closest COM-to-COM separation of Earth and Toutatis will be 1,549,834 $\pm$ 10 km (4.0 lunar distances). We use refined spin-state parameters and the 1995 shape model to generate "movies" that predict the asteroid's rotational motion during its 2004 close approach, in geocentric and inertial frames.**

Key Words: **asteroids; radar; Toutatis.**

1. INTRODUCTION

Asteroid 4179 Toutatis, formerly designated 1989 AC, was discovered by C. Pollas, J.-L. Heudier, R. Chemin, and A. Maury on 1989 Jan. 4 at Caussols, France (Marsden 1989a,b, 1990). The asteroid's orbit ($a = 2.51$ AU, $e = 0.64$, $i = 0.46°$) has the lowest orbital inclination of any known Earth-crossing asteroid except for 1998 MZ ($i = 0.13°$). It is currently in a 3:1 mean-motion resonance with Jupiter (Marsden 1989c, Milani *et al.* 1989), which provides a dynamical pathway for transfer of material from mainbelt orbits near the 3:1 Kirkwood gap into Earth-crossing orbits on time scales of order 10^6 years. Marsden (1970) noted that objects in the 3:1 resonance with Jupiter are prone to enter a temporary 1:4 resonance with Earth, leading to a series of close approaches 4 years apart; Toutatis is doing this now. Toutatis' orbit is one of the most chaotic studied to date (Whipple 1995, Whipple and Shelus 1993), a consequence of the asteroid's frequent close approaches to Earth. There is a broad consensus that Toutatis is in the S taxonomic class (Tholen and Spencer 1992, Howell *et al.* 1994, Lazzarin *et al.* 1994, Lupishko *et al.* 1995, Mukai *et al.* 1997).

0019-1035/99 $30.00

TABLE I
Toutatis Ephemeris

1996				
DOY	Date	RA	Dec	RTT (s)
330	Nov 25	242°	−30°	43
331	Nov 26	234°	−30°	40
332	Nov 27	225°	−28°	38
333	Nov 28	216°	−26°	36
334	Nov 29	207°	−23°	35
335	Nov 30	198°	−19°	36
336	Dec 1	189°	−15°	37
337	Dec 2	182°	−11°	39
338	Dec 3	175°	−8°	41

Note. DOY is day of year, RA is right ascension, Dec is declination, and RTT is echo roundtrip time delay in seconds (equal numerically to the approximate distance in 10^{-3} AU). Entries are for the middle of each date's observations, during which sky motion was no more than 2°.

Delay-Doppler radar imaging during Toutatis' Dec. 1992 close approach (to within 0.024 AU, or 9.4 lunar distances) provided information that is unprecedented for an Earth-crossing object (Ostro *et al.* 1995; see also Zaitsev *et al.* 1993). Hudson and Ostro (1995, hereafter HO95) used a comprehensive physical model to invert the lower-resolution images to estimate the asteroid's detailed shape and inertia tensor, initial conditions for the asteroid's spin and orientation, the radar scattering properties of the surface, and the delay-Doppler trajectory of the center of mass. They found that Toutatis is rotating in a long-axis mode characterized by periods of 5.4 days (rotation about the long axis) and 7.4 days (average for long-axis precession about the angular momentum vector). The inertia tensor is indistinguishable from that of a homogeneous body, and dimensions along the principal axes are within 0.10 km of 1.92, 2.40, and 4.60 km.

The late 1996 approach (Table I) was 50% further than that in 1992. However, prior knowledge of the object's ephemeris and physical characteristics (and the predictability of the progression of Toutatis' delay-Doppler signature (Hudson and Ostro 1996)) greatly simplified the 1996 observations. We carried out nine consecutive days of delay-Doppler and Doppler-only measurements, increasing the radar time base from 3 weeks to 4 years and thereby permitting significant refinements in our knowledge of the asteroid's orbit, spin state, shape, and radar scattering properties. Here we describe the 1996 experiment. We use the HO95 model to refine estimates of the orbit and spin state and to normalize our radar cross sections, thus defining the asteroid's radar reflectivity, which has implications for the object's surface properties. (The high-resolution images from 1992 and 1996 are being used to produce a high-resolution shape model that will be reported later.) Throughout this paper, unless otherwise noted, stated uncertainties are estimated standard errors and are intended to include systematic effects.

2. OBSERVATIONS

Table II describes our radar setups and Table III lists the observations performed on each date. Part of our experiment used continuous-wave (cw) transmissions and produced echo power spectra, which can be thought of as one-dimensional (Doppler-only) images, or brightness scans across the target through a slit parallel to the apparent spin vector. Over the past decade we have found that at Goldstone, cw data can be more reliably

TABLE II
Setups

Baud		RP		Band	Δf		Time/rec
μs	m	(μs)	NCOH	(Hz)	(Hz)	Looks/rec	(s)
Coarse ranging							
11	1650	2805.0	1	356.5	1.393	7	5.0
10	1500	2550.0	1	392.2	1.532	7	4.6
Low-resolution imaging							
1	150	255.0	50	78.43	0.306	1	3.3
High-resolution imaging							
0.125	18.75	31.875	3700	8.479	0.0331	1	30.2
Doppler-only (cw)							
IBM				1000	0.976	29	30
VME				1000	0.244	7	30

Note. The unaliased frequency window, Band, the frequency resolution, Δf, the number of incoherently summed coherent integrations (looks) per data record, and the time per data record are given for each setup. The time resolution (baud, Δt) and code repetition period RP are given for the three time-resolved setups, each of which used a 255-element binary-phase code and a 256-point FFT. NCOH is the number of RP-long time series of voltage samples coherently summed after decoding. Fourier analysis of an RP-long time series of voltages within any given range cell produces a power spectrum, and repetition of that process for each range bin produces a delay-Doppler image that is referred to as one look.

TABLE III
Observations

DOY Date	File	Δt (μs)	Poln 1, 2	OSOD	TXOFFSET Hz	TXOFFSET RBIN	EPH BIN	Start–Mid–Stop (hhmm–hhmm–hhmm)	N	PT kW	RCV	km/ Hz	$\Delta f \times \Delta t$ (m×m)
330	cw	cw	OC,SC	50	cw	cw	cw	1800–1809–1817		495	14	1.29	
Nov 25	33003	11	OC	50	14	0	11	1836–1841–1846	35	490	14	1.29	
	33006	10	OC	50	14	0	11	1858–1904–1910	32	490	14	1.29	
	33008	10	OC	50	14	0	11	1918–1922–1925	54	490	13	1.28	
	33010*	1/8	OC	50	−5	0	31	1945–1948–1951	11	390	13	1.28	43 × 19
331	cw	cw	OC,SC	53	cw	cw	cw	1716–1726–1736		493	13	1.06	
Nov 26	33102*	1/8	OC	53	0	0	31	1748–1754–1800	75	397	13	1.05	35 × 19
	33103	1/8	OC	53	0	0	31	1901–1908–1915	32	397	13	1.04	34 × 19
332	cw	cw	OC,SC	57	cw	cw	cw	1631–1636–1641		495	13	0.909	
Nov 27	33202	10	OC	57	14	0	11	1651–1653–1655	47	487	13	0.907	
	33205*	1/8	OC	57	0	50	81	1714–1747–1820	130	400	13	0.905	30 × 19
	33207	1	OC	57	5	0	13	1824–1827–1830	37	420	13	0.903	
333	cw	cw	OC,SC	57	cw	cw	cw	1531–1536–1541		495	13	0.894	
Nov 28	33304*	1/8	OC	57	0	100	131	1651–1732–1813	161	395	13	0.895	30 × 19
334	cw	cw	OC,SC	57	cw	cw	cw	1436–1441–1446		494	13	0.911	
Nov 29	33402*	1/8	OC	57	0	100	131	1455–1535–1616	154	387	13	0.911	30 × 19
	33403	1/8	OC	57	0	100	131	1619–1637–1656	72	387	13	0.912	30 × 19
335	cw	cw	OC,SC	57	cw	cw	cw	1331–1336–1341		496	13	0.948	
Nov 30	33502*	1/8	OC	57	0	100	131	1357–1437–1518	160	397	13	0.951	30 × 19
	33503	1/8	SC	57	0	100	131	1523–1548–1613	99	397	13	0.955	32 × 19
	33504**	1/8	OC,SC	57	0	60	91	1626–1638–1651	94	397	13	0.958	32 × 19
336	cw	cw	OC,SC	57	cw	cw	cw	1231–1236–1241		495	13	1.03	
Dec 1	33602*	1/8	OC	57	0	100	131	1247–1323–1400	144	396	13	1.04	34 × 19
	33603**	1/8	OC,SC	57	0	60	91	1413–1445–1518	127	396	13	1.05	35 × 19
	33604**	1/8	OC,SC	57	0	60	91	1520–1538–1555	60	396	13	1.05	35 × 19
	33605**	1/8	SC,OC	57	0	60	91	1604–1623–1651	90	396	13	1.06	35 × 19
337	cw	cw	OC,SC	57	cw	cw	cw	1141–1146–1151		495	13	1.20	
Dec 2	33702*	1/8	OC	57	0	100	131	1203–1309–1308	128	446	13	1.22	40 × 19
	33703	1/8	SC	57	0	100	131	1310–1343–1416	128	446	13	1.23	41 × 19
	33704	1/8	OC	57	0	100	131	1418–1532–1646	291	446	13	1.26	42 × 19
338	cw	cw	OC,SC	57	cw	cw	cw	1052–1058–1102		375	13	1.76	
Dec 3	33803*	1/8	OC	57	0	120	151	1117–1208–1259	200	375	13	1.81	60 × 19
	33804	1/8	SC	57	0	120	151	1301–1333–1406	68	375	13	1.88	62 × 19

Note. This table lists all useful data sequences during the 1996 Goldstone observations of Toutatis. DOY is day of year. For each sequence we give the polarization(s) received in channel 1 (or 1 and 2), the OSOD orbit/ephemeris solution identification number (see Section 3), the start–midpoint–stop times of data reception, the average transmitter power, the receiving antenna (DSS-13 or DSS-14), and the km/Hz conversion factor based on our refined estimates of spin state parameters (Table VII). File identification numbers are given for delay-Doppler (ranging and imaging) setups (Table II), which are identified by their delay resolution (Δt). For these files, we give the setup's pixel dimensions in meters, the total number of looks (N) in the file, and the following additional information. The column labeled TXOFFSET lists transmitter offsets inserted to reposition echoes in frequency (with respect to the FFT's zero-frequency element) or in "range" bins (RBIN); EPH BIN is the bin in the range code (the first bin is No. 1) that consequently would contain echo from Toutatis' COM if our ephemeris were perfect. Figure 1 shows sums of images in files flagged by a single asterisk and Fig. 4 shows sums of images in files flagged by two asterisks.

calibrated than delay-Doppler data. (With the exception of the brief cw run that produced the initial radar echo from Toutatis, at Goldstone on Nov. 27, 1992, no Goldstone or Arecibo cw observations were done during that apparition.)

Our goal in doing cw work was to measure the asteroid's radar cross sections in the same circular polarization as transmitted (the SC sense) and in the opposite (OC) sense. During the observations, OC and SC echo power spectra were formed simultaneously, with each of two data-acquisition systems that operated in parallel: an IBM system that had been used for several years and a new VME system that was just being debugged. We took about 10 min of cw data daily. The cw setups were designed to place only a handful of cells on Toutatis, because coarser frequency resolution led more rapidly to Gaussian noise statistics (desirable for clean background removal and accurate normalization), and because the goal of our cw runs was to obtain accurate disc-integrated radar cross sections, not spatial resolution.

During the cw runs, the transmitter was switched between two frequencies, and the data collected were sorted into two corresponding groups of power spectra and then summed. Each sum had echo at a different frequency, so either sum contained a

sample of the echo-free noise background at the frequency of the other sum's echoes. Such a "frequency-hopped" data set permits reliable background removal and data normalization. Problems with calibration and our data-tagging protocol afflicted the cw observations on our first two dates, but we have confidence in the last seven dates' cw results.

Most of our observations used a time-modulated waveform to obtain resolution in time-delay as well as Doppler frequency. The result is a two-dimensional image that cuts the target with two orthogonal sets of parallel planes; one set is parallel to the plane of the sky (POS), and the other set is parallel to the plane that contains both the target's apparent spin vector and the radar. Each delay-Doppler observation used a repetitive, binary-phase-coded cw waveform (e.g., Ostro 1993 and references therein) with a 255-element code and one of four time resolutions, or "bauds" ($\Delta t = 11$, 10, 1, or 0.125 μs; Table II). Our daily high-resolution imaging setup had pixel dimensions 0.125 μs $\times$ 33 mHz. The most important steps in real-time processing of digitized samples of the received signal's voltage were decoding via cross-correlation with the transmitted code and spectral analysis with a fast Fourier transform of length LFFT = 256. This procedure produced 256 $\times$ 255 arrays of echo power. Each array's unaliased frequency window equals $1/(\mathrm{RP} \times \mathrm{NCOH})$, where the code repetition period, $\mathrm{RP} = 255\Delta t$, defines the waveform's time-delay window, and NCOH is the number of RP-long time series of decoded voltage samples that were coherently summed prior to Fourier analysis. A power spectral estimate for each delay cell is obtained from coherent analysis of $\mathrm{TCOH} = \mathrm{RP} \times \mathrm{NCOH} \times \mathrm{LFFT}$ seconds of data; we refer to such an image as one look. Spectral estimation noise is χ^2 distributed and the fractional rms fluctuation in a sum of N looks is $1/\sqrt{N}$; echo "self-noise" dominates receiver noise in our images. Thus, fine frequency resolution requires long coherence time TCOH, and low noise requires incoherent summation of many looks. However, long integrations are undesirable if the resolution is degraded by smearing from either the target's rotation or its translational motion with respect to the delay-Doppler prediction ephemeris, which is used to drift the sampling time base to maintain coregistration of echoes from any given range bin, and to tune the receiver to the Doppler-shifted echo. The Doppler-prediction error $\Delta\nu_{\mathrm{eph}}$ defines the rate of change of the delay-prediction error $\Delta\tau_{\mathrm{eph}}$ and hence the rate of delay smearing,

$$d\Delta\tau_{\mathrm{eph}}(t)/dt = -\Delta\nu_{\mathrm{eph}}(t)/F_{\mathrm{TX}}, \qquad (1)$$

where F_{TX} is the transmitter frequency. For Toutatis, with a ponderously slow rotation and thus a very narrow echo bandwidth, long coherent and incoherent integrations are needed to achieve fine Doppler resolution and small noise fluctuations. Therefore very accurate Doppler-prediction ephemerides are required and, as described below, refining our ephemerides was a primary objective during the first three observation days.

In 1992, the single Goldstone cw run and 6-cm Yevpatoria–Effelsberg observations (Zaitsev *et al.* 1993) revealed that Toutatis' OC echoes are several times stronger that its SC echoes, and some coarse-resolution Arecibo images hinted that OC and SC delay-Doppler images do not look very different. In 1996 we used our high-resolution setup to do OC imaging daily, SC imaging on 2 days, and simultaneous SC and OC imaging on 2 days (Table III).

All our observations used Goldstone's 70-m antenna, DSS-14, for transmitting a signal with nominal frequency 8510 MHz (X-band, $\lambda = 3.52$ cm). The Goldstone radar system is described by Priest (1993); see Fig. 1 of Ostro *et al.* (1996) for a summary block diagram.

On the first day, our initial setups (cw, 10-μs ranging, and 11-μs ranging) alternated DSS-14 between transmitting and receiving configurations every roundtrip time (45 s). After these single-antenna, "monostatic" runs we did some 10-μs runs in a bistatic mode, transmitting continuously from DSS-14 and receiving continuously at DSS-13, a 34-m antenna 22 km away. The combination of short roundtrip time delays (Table I) and the enormous strength of the echoes made the bistatic mode preferable for this experiment, and it was used for the rest of our observations. At DSS-13, the output from the front end amplifier, a low-noise maser, is tuned continuously to remove the predicted Doppler shift and the signal is converted down to a 50-MHz intermediate frequency, which is sent over a fiber-optic cable to DSS-14, where it is processed as in monostatic observations. The signal propagation time from DSS-13 to DSS-14, 138.187 μs, is taken into account by the data-acquisition system that defines the coordinate system for delay-Doppler power arrays, which are accumulated in real time.

Figure 1 shows summed images from the nine OC files (one from each date; see Table III) used in the analyses discussed in the next two sections. These files were obtained bistatically with the high-resolution setup in Table II and contain between 11 and 200 looks.

3. ASTROMETRY AND ORBIT REFINEMENT

With any repetitive "ranging" waveform, the time-delay correction to the ephemeris is determined modulo the RP. The RP of each of our long-baud setups was an order of magnitude larger than the *a priori* delay uncertainty before our experiment began (115 μs), and together those setups completely eliminated any ambiguity in our delay measurements on the first observation day. Thereafter, even the short-baud RP was large enough to eliminate any ambiguity.

Our delay/Doppler/pointing prediction ephemerides were generated at Goldstone with JPL's On-Site Orbit Determination program (OSOD). On the first day (Nov. 25), we measured +5-Hz and +63-μs corrections to orbit OSOD-50 and incorporated those results in calculation of a new orbit solution, OSOD-53. On the second day, we measured 0-Hz and -8.75-μs corrections to OSOD-53 and generated a new solution, OSOD-57. On the third day, we measured 0-Hz and -0.25-μs corrections to solution 57 and built a new solution (59). However,

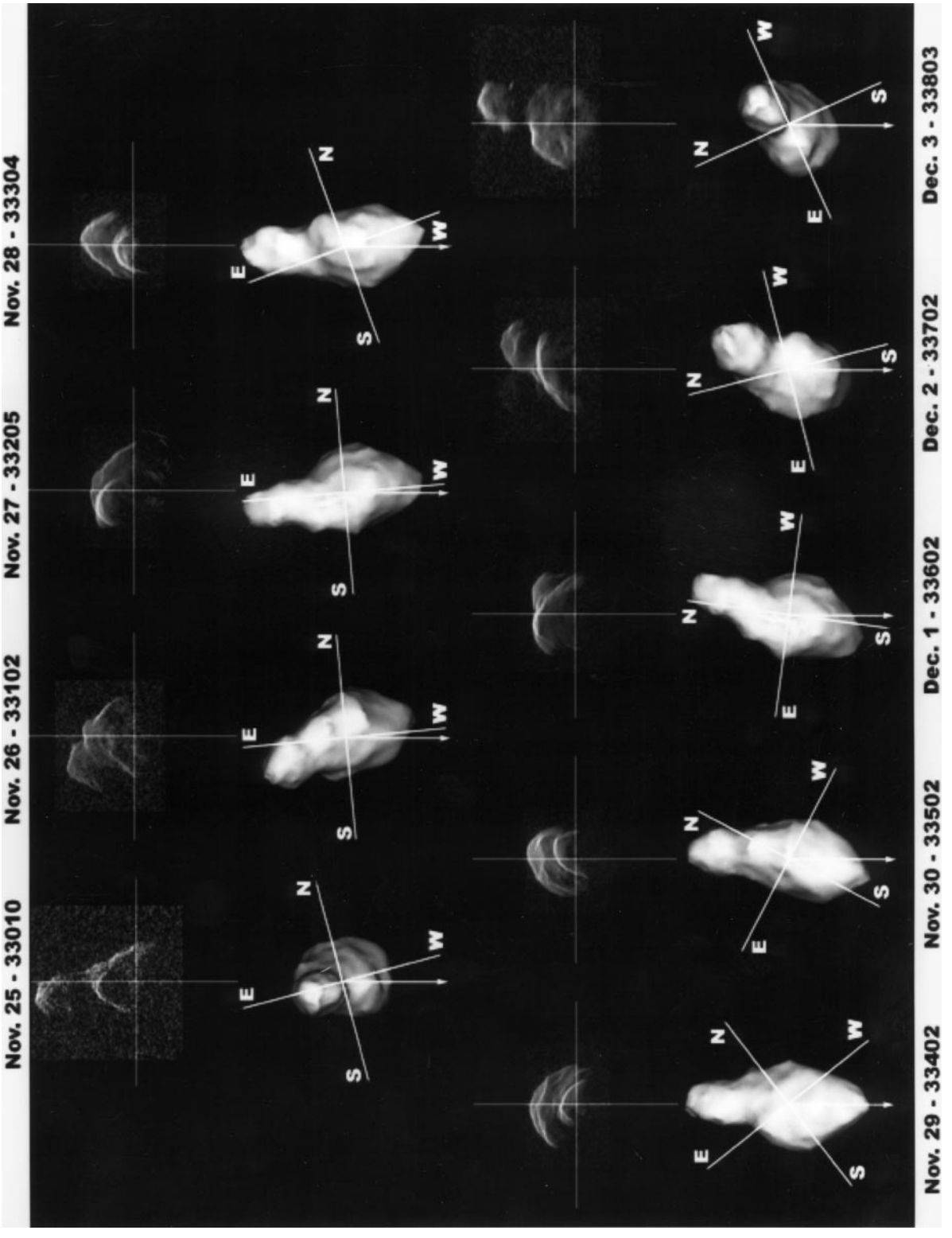

FIG. 1. High-resolution delay-Doppler images from each observation date (see Table III) and corresponding plane-of-sky (POS) appearance of Toutatis. Each image is a sum of all looks in the indicated file. Gray scales have been chosen to emphasize brightness contrast. The cross-hairs are 5 km long and centered on Toutatis' center of mass. The radar images are plotted with time delay (range) increasing from top to bottom and Doppler frequency (radial velocity) increasing from left to right. The km/Hz conversion factors in Table III have been used. In the POS images, the HO95 model is rendered with a Lambertian scattering law, with the viewer and illumination source colocated. The cross-hairs are aligned north–south and east–west on the plane of the sky. In each POS frame, the arrow is parallel to the POS projection of the instantaneous spin vector.

TABLE IV
Delay-Doppler Astrometry

UTC epoch of echo reception	Time delay (UTC μs)			Doppler frequency (Hz)		
	Estimate	±	Resid.	Estimate	±	Resid.
1996 Nov 25 19:50:00	43021144.95	0.25	0.93	335217.755	0.07	−0.14
1996 Nov 26 18:00:00	40128415.09	0.25	−0.09	283557.367	0.07	0.07
1996 Nov 27 17:50:00	37686307.90	0.25	−0.21	206061.474	0.07	−0.09
1996 Nov 28 17:30:00	36072841.55	0.25	−0.90	117850.312	0.07	−0.04
1996 Nov 29 15:40:00	35385422.19	0.25	0.63	36193.593	0.07	−0.08
1996 Nov 30 14:40:00	35551769.77	0.25	−0.77	−54016.239	0.07	−0.03
1996 Dec 01 13:20:00	36572924.18	0.25	−0.12	−135658.745	0.07	−0.06
1996 Dec 02 13:10:00	38471794.20	0.25	0.20	−216056.675	0.07	−0.04
1996 Dec 03 12:10:00	40997833.07	0.25	0.50	−276563.595	0.07	−0.04

Note. Astrometry corresponds to 8510-MHz transmission from DSS-14, reflection from Toutatis' COM, and reception at DSS-13. Each antenna's reference point is the intersection of the azimuth and elevation axes. Residuals are with respect to OSOD Solution 66 (Table V). The range equivalent of 1 μs is 150 m and the radial velocity equivalent of 1 Hz is 18 mm s^{-1}.

the differences between solutions 59 and 57 for the balance of our experiment were never as large as 1 μs (75 m) or 0.02 Hz (0.4 mm/s). Since that Doppler error would cause delay smear of less than 0.05 μs (8 m) over the longest remaining Goldstone track, we stayed with solution 57. The largest absolute values of corrections to OSOD-57 during the last 6 days were 0.02 Hz and 1.7 μs. Our high-resolution sequences (Table III), which used bauds of 0.125 μs (19 m), are smeared in range by 3 m or less.

Table IV lists delay-Doppler astrometry from each day of the 1996 experiment. Radar astrometry is best referred to echoes from the target's center of mass (COM). We identified the COM pixel in each of the 1996 images by fitting to them image templates based on the HO95 model. (The cross-hairs in Fig. 1 are centered on the COM.) Those measurements, along with optical astrometry and 1992 radar astrometry, yield orbit solution OSOD-66 (Table V). Integration of that orbit forward and backward in time reveals the close planetary approaches in Table VI. The 3-σ uncertainties in the 1992 and 1996 close-approach distances are less than three times the range resolution (19 m) of the radar setups used in those years. The 3-σ uncertainty in the 2000 close-approach distance is about 1/4 of Toutatis' shortest overall dimension.

TABLE V
Orbit (OSOD Solution 66)

Epoch (TDB)	2450540.5, 1997 Apr 2.0
Perihelion passage time (TDB)	1996 Nov. 10.99819534 (66)
Perihelion distance (AU)	0.9204650369 (78)
Eccentricity	0.6335693350 (30)
Longitude of ascending node (deg)	128.208210 (235)
Argument of perihelion (deg)	274.826045 (235)
Inclination (deg)	0.46972268 (373)

Note. Toutatis' heliocentric orbital elements and formal 3-standard-deviation uncertainties (in parentheses, in units of the last decimal place), estimated using our radar astrometry (Table IV), the radar astrometry reported by Ostro *et al.* (1995), and 588 optical astrometric observations from 1988 through March 1997. Elements are in the coordinate frame of the JPL planetary ephemeris DE-405 (ICRF93/J2000, a quasar-based radio frame, generally within 0.01 arcs of the optical FK5/J2000 frame). Angular orbital elements are referred to the ecliptic and mean equinox of J2000. Weighted rms residuals are 0.98 arcs, 0.10 Hz (1.8 mm s^{-1} in radial velocity) and 0.49 μsec in time delay (73 m in range).

Positional uncertainties increase away from the decade spanned by the astrometric data set because of a combination of factors. There is a three-dimensional probability density function associated with any predicted position, and the locus of a given probability density can be thought of as a surface whose shape generally can be approximated by an ellipsoid. A linearized covariance mapping or Monte Carlo simulations can be used to approximate the evolution of possible trajectories, and one can think of, say, the 3-σ error ellipsoid as bounding the set of possible trajectories at the 3-σ level (e.g., Muinonen 1996, 1998). As time passes, members of the set of possible trajectories diverge from each other because of errors in the initial conditions (position and velocity vectors) and because of uncertainties in the varying gravitational environment. This gravity gradient effect across the ellipsoid is exaggerated at any close approach, so the ellipsoid swells at those times—hence the rapid enlargement of uncertainties beyond the very close approaches in 1376 and 2069. The ellipsoid expands even more after the very close approach in 2562; the distance uncertainty for a Mars approach in 2570 is several AU.

The long-term danger of asteroid collisions with Earth has begun to attract attention. In this context, we note that the uncertainty in a close-approach distance is a one-dimensional statistic that is not sufficient for calculation of a collision probability, which is a three-dimensional problem (Yeomans and Chodas 1994), a solution of which can be visualized as follows. Imagine that the probability density function is an extended gaseous cloud of probability whose integral is unity, and that at a close approach, the cloud is "deposited on" the plane that contains the

TABLE VI
Close Planetary Approaches

TDB epoch of close approach				Body	Distance (AU)	3-σ Uncertainty		Intersection ellipse (sigmas)
(Julian Date	Year	Mon	Day)			AU	km	
2215525.12466	1353	Oct	19.62466	Venus	0.08977	±0.025	3700000	2.1E6
2223862.30223	1376	Aug	16.80223	Earth	0.01566	±0.00009	14000	1.2E6
2228100.63371	1388	Mar	25.13371	Venus	0.08329	±0.00002	2900	1.4E7
2235058.47370	1407	Apr	13.97370	Mars	0.03993	±0.00035	53000	7.9E5
2243705.73094	1430	Dec	16.23094	Earth	0.08376	±0.00014	21000	3.8E4
2245059.78967	1434	Aug	31.28967	Earth	0.01647	±0.000012	1700	2.9E6
2253612.36650	1458	Jan	29.86650	Mars	0.03202	±0.000009	1300	1.2E6
2279024.70956	1527	Aug	29.20956	Earth	0.04955	±0.000011	1700	2.8E6
2280466.60814	1531	Aug	10.10814	Venus	0.09258	±0.000011	1600	2.3E6
2290383.48397	1558	Oct	03.98397	Mars	0.03829	±0.0000035	530	2.5E6
2297286.98357	1577	Aug	28.48357	Earth	0.01422	±0.0000007	110	2.9E6
2321976.55755	1645	Apr	03.05755	Mars	0.07741	±0.0000041	620	4.8E6
2347026.55280	1713	Nov	03.05280	Earth	0.02185	±0.00000007	11	1.1E6
2382091.02502	1809	Nov	04.52502	Mars	0.08536	±0.00000010	15	4.9E6
2396404.30305	1849	Jan	11.80305	Venus	0.09706	±0.00000002	2	1.9E7
2397856.07934	1853	Jan	02.57934	Earth	0.07119	±0.00000012	18	1.8E6
2403373.00756	1868	Feb	10.50756	Mars	0.05419	±0.00000006	9	3.2E6
2407705.16281	1879	Dec	21.66281	Earth	0.06878	±0.00000014	22	1.7E6
2411991.49187	1891	Sep	15.99187	Mars	0.05525	±0.00000004	6	6.6E6
2423144.32916	1922	Mar	30.82916	Venus	0.08870	±0.000000030	4.4	4.4E7
2448964.73342	1992	Dec	08.23342	Earth	0.02415	±0.0000000003	0.044	2.5E8
2450417.45333	1996	Nov	29.95333	Earth	0.03542	±0.0000000003	0.043	3.8E8
2451848.68624	2000	Oct	31.18624	Earth	0.07386	±0.000000003	0.43	7.9E7
2453278.06705	2004	Sep	29.56705	Earth	0.01035	±0.000000064	9.6	1.0E6
2454780.01610	2008	Nov	09.51610	Earth	0.05025	±0.00000034	51	1.2E6
2456273.77842	2012	Dec	12.27842	Earth	0.04634	±0.0000030	440	8.0E5
2477056.14532	2069	Nov	05.64532	Earth	0.01985	±0.0000017	250	1.3E6
2569442.96917	2322	Oct	18.46917	Earth	0.06032	±0.0031	460000	1.8E6
2620555.27783	2462	Sep	25.77783	Earth	0.03660	±0.0071	1100000	1.7E5
2645877.92396	2532	Jan	25.42396	Earth	0.09004	±0.018	2600000	4.2E6
						+0.012	1800000	
2657084.69373	2562	Oct	01.19373	Earth	0.00250			2.3E5
						−0.0014	200000	

Note. Close approaches to within 0.1 AU of inner Solar System bodies, along with 3-σ uncertainties in the close-approach distance. (Toutatis is at least 1 AU from Jupiter throughout this period.) These formal uncertainties may underestimate true uncertainties by factors of several for encounters centuries away from the present. The error distribution is symmetrical for all close approaches listed here except for the 2562 approach, for which it is highly asymmetrical. The final column gives the uncertainty ellipse that intersects the center of the planetary body, in sigmas; note that the 10000-σ uncertainty ellipse does not encompass the planetary body for any of these close approaches. Toutatis' collision probability with any planet is zero throughout this period. See text.

asteroid–Earth line and is normal to the asteroid's geocentric velocity, so that plane is "painted" with probability whose integral is unity. The error ellipsoid then becomes an error ellipse which represents the marginal probability density function describing the probability that the object will at some time pass through a given point on the impact plane. Earth's intersection with this plane is a circle, and to first order, the probability of Earth impact is computed simply by integrating the marginal probability density function over the area of this circle. For each approach in Table VI, we find that Toutatis' collision probability is zero.

It is interesting that Toutatis' Sep. 29, 2004, approach to 0.01 AU (4.0 Earth–Moon distances) is the asteroid's closest approach to any planet during a time period longer than a millennium, with the next closer approach (0.0036 AU) not until 2562. Also note the curious pre/post-1992 asymmetry in the frequency of Mars and Venus close approaches.

4. REFINEMENT OF SPIN STATE

The HO95 Toutatis model has a shape defined by 3196 triangular surface facets and a scattering law with parameters for the angular dependence and the strength of the surface's radar brightness. The non-principal-axis spin state is specified by eight parameters: the Euler angles that define the asteroid's orientation with respect to ecliptic coordinates at a specified epoch, the projections of the spin vector along the principal axes of inertia at that epoch, and the ratios of the short- and intermediate-axis moments of inertia to the long-axis moment. Using the 1995 shape

TABLE VII
Spin State

t_0	11 Dec. 1992, 9:21 UTC
ϕ_0	-103 ± 3 degrees
θ_0	97 ± 3 degrees
ψ_0	-134 ± 3 degrees
ω_{0s}	20.7 ± 0.1 degrees/day
ω_{0i}	31.3 ± 0.1 degrees/day
ω_{0l}	98.0 ± 0.1 degrees/day
I_s/I_l	3.22 ± 0.01
I_i/I_l	3.09 ± 0.01

Note. Toutatis' rotation is specified by the tabulated initial conditions. At the epoch t_0, the Euler angles $(\phi_0, \theta_0, \psi_0)$ give the initial orientation of the principal axes of inertia with respect to ecliptic coordinates. The evolution of that orientation is defined by the projections of the instantaneous spin vector **W** along the short, intermediate, and long principal axes $(\omega_{0s}, \omega_{0i}, \omega_{0l})$, and the ratios of principal moments of inertia with respect to those axes. The uncertainties are conservative estimates based on simulations with the HO95 model. Compared to the HO95 spin state, the uncertainty in the three initial angles stays the same, but the uncertainties in the spin vectors and moment ratios decrease by an order of magnitude. The spin state parameters define the direction of Toutatis' angular momentum vector as ecliptic longitude, latitude $= 180^\circ, -52^\circ$.

model to analyze the large set of optical lightcurves presented by Spencer *et al.* (1995), Hudson and Ostro (1998) estimated the asteroid's Hapke (1993) parameters and also obtained a slight refinement of the spin state.

In our analysis of the 1996 radar images, we held the HO95 shape model and radar scattering properties constant while adjusting the spin state parameters. We began by examining fits to the 1996 images using both the original "radar-only" spin state (HO95) and the "radar + optical" spin state (Hudson and Ostro 1998). We found that the lightcurve-refined spin state did considerably better in predicting the orientational sequence displayed in the 1996 images. Incorporating those images in the least-squares solution reduces uncertainties in the initial spin vector components and the moment ratios by an order of magnitude. Table VII shows the resultant spin-state parameters along with uncertainties estimated by randomly perturbing the spin-state parameters by various amounts and observing the effect on the fits. In Fig. 1, each delay-Doppler image is accompanied by a rendering of the HO95 shape model in the POS orientation predicted for the image's midpoint-epoch using the Table VII spin state.

Figure 2 illustrates our predictions for the orientation of Toutatis in inertial and geocentric frames during its very close approach in 2004. The uncertainty in these predictions can best be expressed in terms of the uncertainties in the components of the asteroid's rotation, which is a combination of a slightly wobbling rotation about the long principal axis every 5.367 ± 0.01 days and a uniform precession of that axis about the angular momentum vector every 7.420 ± 0.005 days. The latter motion is what primarily determines the inertial orientation of the long axis, while the former motion primarily determines the orientation of the other two axes about the long axis. Propagation of current uncertainties in these periods to the 2004 close approach gives uncertainties of about 90° in the phase of the long-axis within its precession pattern and about 180° in the orientation of the shorter axes about the long axis.

5. SURFACE CHARACTERISTICS FROM DUAL-POLARIZATION RESULTS

5.1. Disc-Integrated Properties

Table VIII lists our single-date and experiment-average estimates of disc-integrated radar properties from the cw observations, including the SC/OC ratio μ_C, the OC radar cross section σ_{OC}, and the OC radar albedo, defined by

$$\hat{\sigma}_{OC} = \sigma_{OC}/A_{proj}. \quad (2)$$

The tabulated projected areas A_{proj} use the spin state parameters in Table VII and the HO95 shape model. Toutatis' OC albedo depends on orientation, as expected for any nonspherical target with a limb-darkened angular backscattering law. The HO95 modeling showed Toutatis' limb-darkening to be slightly more than Lambertian (see below). Toutatis' mean OC albedo, 0.24, is several times that of the Moon. (A spherical object with the same scattering behavior as the HO95 model would have an albedo of 0.21, and that value probably is more suitable for comparison with other solar system targets.) As discussed below, radar reflectivity depends primarily on near-surface bulk density, but quantitative interpretation of $\hat{\sigma}_{OC}$ depends on the nature of the radar scattering. Toutatis' polarization signature constrains the scattering process and hence the surface characteristics, as follows.

FIG. 2. Toutatis' orientation during its 2004 close approach (Table VI), predicted using the spin state in Table VII. The HO95 shape model is rendered with a Lambertian scattering law, with the viewer and illumination source colocated in (a) geocentric and (b) inertial frames. The sequence in (a) shows the appearance of the asteroid on the plane of the sky (POS), with north toward the top. Time increases from left to right and from top to bottom in 6-h increments between frames, so each row of four frames represents 1 day. The sequence begins at Sep. 27.0. Because Toutatis rotates slowly and is moving rapidly on the sky during this time, the orbital contribution to the apparent rotation is quite significant. The sequence in (b) uses an inertial frame, and here all the orientational motion is due to the asteroid's intrinsic rotation. At the initial epoch, the lines of sight in (a) and (b) are identical; differences between later corresponding frames of (a) and (b) are due to the asteroid's POS motion (about 120° during this time).

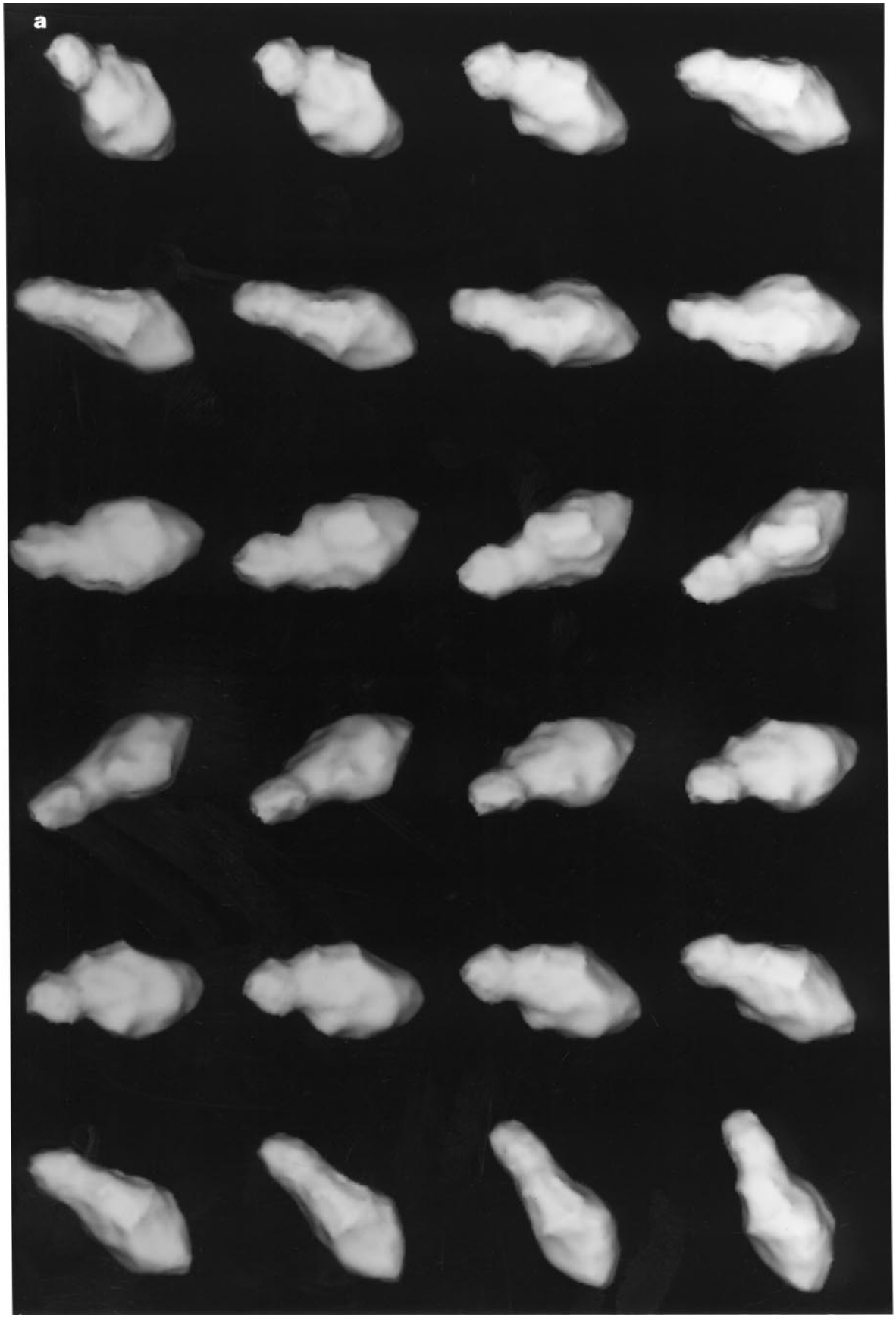

FIG. 2—*Continued*

FIG. 2—*Continued*

TABLE VIII
Disc-Integrated Properties

1996 DOY	Date	μ_C	σ_{OC} (km^2)	A_{proj} (km^2)	$\hat{\sigma}_{OC}$
332	Nov 27	0.30 ± 0.02	1.41 ± 0.16	6.55	0.22 ± 0.02
333	Nov 28	0.30 ± 0.01	1.39 ± 0.14	6.03	0.23 ± 0.02
334	Nov 29	0.27 ± 0.03	1.61 ± 0.25	6.66	0.24 ± 0.04
335	Nov 30	0.28 ± 0.01	1.48 ± 0.15	6.01	0.25 ± 0.02
336	Dec 1	0.28 ± 0.01	1.52 ± 0.15	6.31	0.24 ± 0.02
337	Dec 2	0.29 ± 0.01	1.44 ± 0.14	5.13	0.28 ± 0.03
338	Dec 3	0.29 ± 0.02	0.82 ± 0.08	4.00	0.20 ± 0.02

Mean values

SC/OC ratio, μ_C	0.29 ± 0.01
OC albedo, $\hat{\sigma}_{OC}$	0.24 ± 0.03
SC albedo, $\hat{\sigma}_{SC}$	0.070 ± 0.01
TC albedo, $\hat{\sigma}_{TC}$	0.31 ± 0.04
Geom. albedo	0.078 ± 0.010

Note. Results of cw observations (see text and Table III). DOY is the day of year. Here the total-power radar albedo is $\hat{\sigma}_{TC} = \hat{\sigma}_{OC} + \hat{\sigma}_{SC}$ and the geometric albedo equals $\hat{\sigma}_{TC}/4$. A sphere with Toutatis' radar scattering properties would have $\hat{\sigma}_{OC} = 0.21$.

Single back-reflections from appropriately oriented, smooth surface elements much larger than the wavelength would give $\mu_C = 0$. Multiple scattering generally gives $\mu_C \sim 1$. For example, Liou and Schotland (1971) showed that the linear polarization ratio $\mu_L = OL/SL$, which generally is much less than μ_C, is about 0.8 for twice-scattered radiation from irregular particles with size parameter ($X = \text{circumference}/\lambda$) of order unity. Single scattering from nonspherical particles with X comparable to or larger than unity (or from rough surface elements) gives intermediate μ_C, with the value depending on particle shape, orientation, electrical properties, and surface structure (especially the presence of curvature radii $\leq\lambda$). The singly scattered echo from the extreme case of randomly oriented dipoles would have $\mu_L = 1/3$ and $\mu_C = 1$ (Long 1965). Empirical studies (Sassen 1974, 1975, McNeil and Carswell 1975, Pal and Carswell 1977, Schotland *et al.* 1971) and theoretical studies (Cuzzi and Pollack 1978) indicate that irregularly shaped rocks give $\mu_L > 0.3$; again, μ_C would be much higher.

Toutatis' mean circular polarization ratio, 0.29 ± 0.01, is close to the average value for NEAs: the 29 objects with ratios listed by Ostro *et al.* (1991a) have a mean and rms dispersion of 0.30 ± 0.22. On the other hand, the corresponding numbers for mainbelt asteroids (MBAs) are half as large, and almost all radar-detected MBAs have $\mu_C \leq 0.3$.

Observations of the Moon, Mercury, Venus, and most of Mars except for Tharsis and Elysium give disc-integrated $\mu_C \leq 0.1$ (Harmon and Ostro 1985 and references therein), that is, much lower than Toutatis' value. However, this sort of comparison can be misleading, because those objects backscatter much more specularly than Toutatis, producing a very bright OC echo at the center of the target disc. This quasi-specular OC glare, due to back-reflections from smooth, gently sloped surface elements, is superposed on a weaker, diffuse component that contains both OC and SC power and obeys a scattering law ($d\sigma/dA$, with dA an element of surface area) that has a $\cos^n\theta$ dependence with n typically between 1 and 1.5 (Stacy 1993, Ostro 1993). Diffuse scattering dominates close to the limbs, where most values of μ_C measured for the Moon and inner planets are between 0.3 and 0.6 (Stacy *et al.* 1997, Harmon and Ostro 1985 and references therein), that is, comparable to or higher than Toutatis' value.

5.2. Proportions of Echo Components with Different Polarization Ratios

Let us examine how Toutatis' μ_C constrains the relative contributions from multiple scattering (we assume $\mu_C = 1$), single-scattering from smooth surface elements (we assume $\mu_C = 0$), and scattering from irregular particles (intermediate μ_C). The time-averaged polarization state of a narrowband signal is conveniently described by its four-element Stokes vector (e.g., Guenther 1990). When several echo components having no permanent phase relation between them are combined, the Stokes vector for the mixture is the sum of the components' respective Stokes vectors (Chandrasekhar 1960). Two of the Stokes vector's elements deal with linear polarization and are irrelevant to this discussion, so we ignore them and use a two-element Stokes vector. When normalized to the total echo power, the first element is unity and the second element is $(\mu_C - 1)/(\mu_C + 1)$. Suppose that the jth echo component has circular polarization ratio μ_j and contributes a fraction F_j of the power, so its two-element Stokes vector $\mathbf{S}_j$ has elements $1, (\mu_j - 1)/(\mu_j + 1)$. Then the two-element Stokes vector for the sum of three components will be

$$\mathbf{S}_{NET} = \sum F_j \mathbf{S}_j \tag{3}$$

and the net μ_C will be

$$\mu_{NET} = \frac{1 + \sum(F_j)(\mu_j - 1)/(\mu_j + 1)}{1 - \sum(F_j)(\mu_j - 1)/(\mu_j + 1)}, \tag{4}$$

where all summations are from 1 to 3.

We consider the net polarization ratio μ_{NET} for contributions from three components with μ_C equal to 1, 0, and μ_3. Figure 3 plots contours of constant μ_{NET} on a ternary diagram. At each point in the diagram, $F_1 + F_2 + F_3 = 1$. F_j is unity at the vertex labeled $\mu_C = \mu_j$ and zero on the opposite side. Contours of constant F_j are parallel to that side. The solid lines are contours of $\mu_{NET} = 0.29$ and are plotted for μ_3 equal to 0.3, 0.5, and 0.7. If $F_3 = 0$ (the left side of the triangle), the $\mu_C = 1$ component and the $\mu_C = 0$ component contribute 45 and 55% of the echo power, respectively; these are the maximum percentages of the echo power that can be due to multiple scattering or smooth-surface backreflections, respectively. The percentages of echo from those components decrease as the percentage of echo with μ_3 increases. The bottom of the triangle gives the trade-off between percentages of the $\mu_C = 0$ and $\mu_C = \mu_3$ echo if there is no

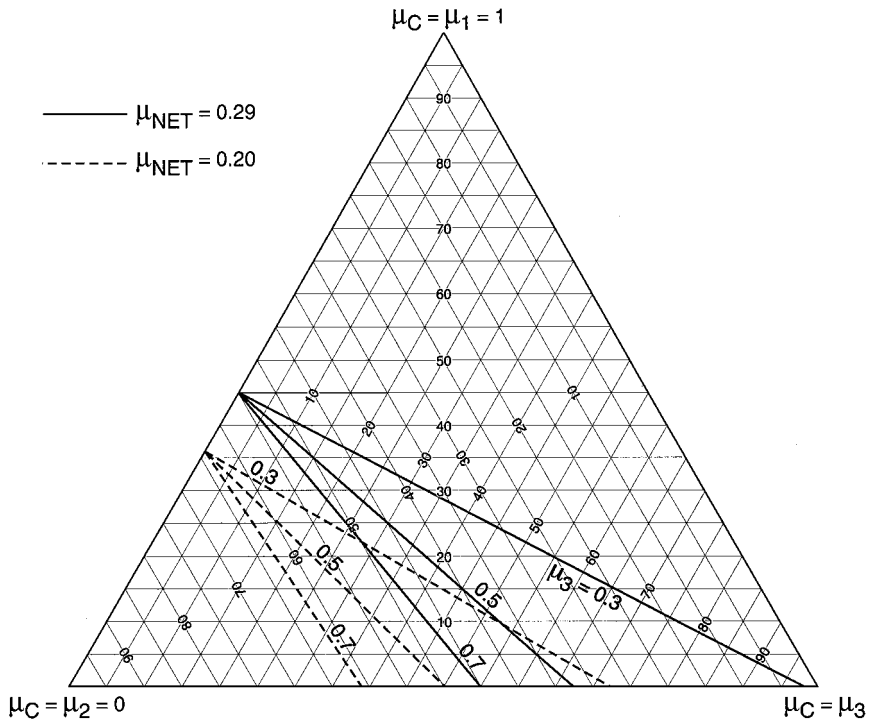

FIG. 3. Polarization "mixtures." The solid lines indicate proportions of echo power from three components with different circular polarization ratios (1, 0, and $\mu_3 = 0.3$, 0.5, or 0.7) that yield a net ratio, $\mu_{\rm NET}$, equal to Toutatis' mean value, 0.29. The dashes lines correspond to $\mu_{\rm NET} = 0.20$, as seen on echo leading edges. The portion of power from any component is zero on the side opposite that component's vertex and increases linearly to 100% at that vertex, as indicated by the faint background lines.

$\mu_{\rm C} = 1$ echo.The field of possibilities in this figure is constrained by the radar data as follows.

5.3. Dual-Polarization Images

Interesting aspects of Toutatis' radar signature can be seen in polarization ratio images formed from simultaneously acquired, high-resolution SC and OC images on Nov. 30 and Dec. 1 (Fig. 4). Apart from their several-fold difference in strength, the SC and OC images look similar. The ratio is very uniform over each image, and nearly all pixels have values between 0.2 and 0.4. In contrast with the abundance of $\mu_{\rm C}$ features evident in delay-Doppler and Doppler-only images of the terrestrial radar targets [e.g., the high-$\mu_{\rm C}$ signatures of some lunar crater walls and ejecta blankets (Stacy 1993, Thompson *et al.* 1981) and very high-$\mu_{\rm C}$ regions on Mars (Harmon and Ostro 1985) and Venus (Haldemann *et al.* 1997)], evidence for localized $\mu_{\rm C}$ anomalies on Toutatis is lacking. However, note the clustering of lower values at some of the echoes' leading edges. We understand this characteristic as due to OC echo from smooth facets that face the radar preferentially where the mean surface is normal to the line of sight. (Note from Fig. 1 that there is a lot of "flat" radar-facing surface area on those dates.) The decrease in $\mu_{\rm C}$ at echo leading edges is very subtle, especially in comparison to the signatures of the inner planets noted above. Toutatis' smooth-surface component probably has relatively less exposure or is relatively unreflective compared to other structural components, or both.

Additional evidence for a smooth-surface component is provided by estimates of Toutatis' OC and SC scattering laws based on the HO95 shape model, the disc-integrated results in Table VIII, and the OC and SC images reported here. The scattering law is homogeneous and varies as $\cos^n\theta$, with $n_{\rm OC} = 3.0 \pm 0.5$ and $n_{\rm SC} = 2.5 \pm 0.5$. That is, the limb-darkening appears to be slightly greater in the OC polarization, as would be expected if some of the OC echo is due to single backreflections from smooth surface elements.

5.4. Radar Penetration Depth

To what degree might our radar echoes be probing Toutatis' subsurface? The one-way $1/e$ power absorption length is (e.g., Hapke 1993)

$$L = \lambda/4\pi \left\{(K_r/2)[(1+\tan^2\delta)^{1/2} - 1]\right\}^{1/2} \qquad (5)$$

or, provided that $\tan\delta \ll 1$,

$$L = \lambda/2\pi K_r^{1/2} \tan\delta, \qquad (6)$$

where the complex dielectric constant is

$$K = K_r + iK_i \qquad (7)$$

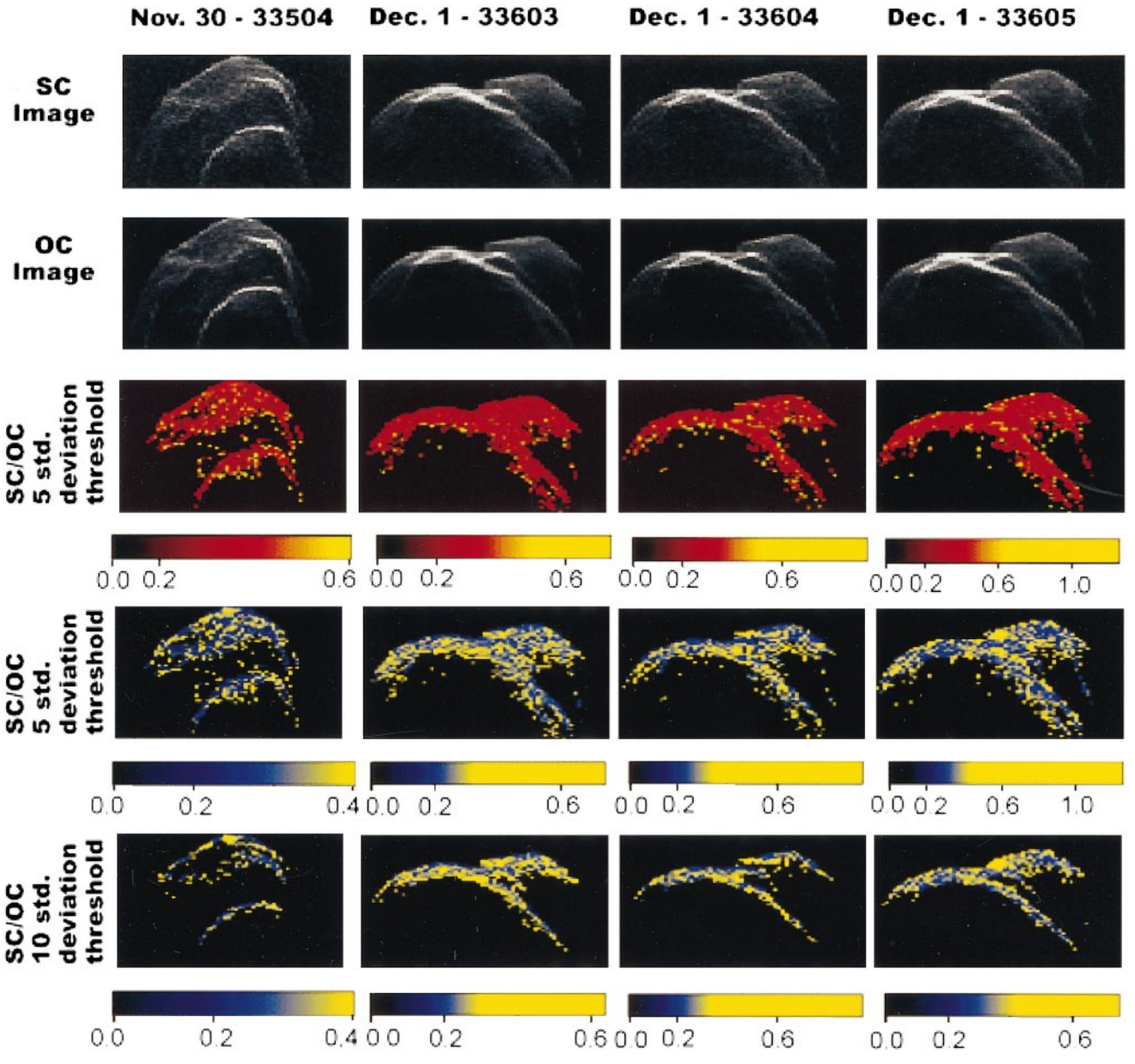

FIG. 4. Sums of simultaneously acquired SC and OC images from the indicated files, along with ratio images obtained by calculating $\mu_C = \text{SC/OC}$ for each pixel containing both SC and OC echo power no less than a particular threshold. Each SC and OC image is the sum of between 60 and 127 looks (Table III), so the noise statistics are almost Gaussian, and the 1-σ error interval for any pixel's μ_C is given by Fieller's Theorem (Finney 1964). The fractional standard error in the ratio for any given pixel with a nonzero value is approximately the reciprocal of the threshold, which was either 5 or 10 standard deviations (sigma), as indicated. The 5-σ-threshold images are shown twice, with two different color maps: the "red" map shows that almost all pixels have μ_C between 0.2 and 0.4, and the yellow-blue map lets the lowest-μ_C pixels be identified. Except for file 33605 (right-hand column), the entire 1996 experiment used transmission of right circular polarization (RCP) and reception of LCP, RCP in channels 1,2. File 33605 used the same receiver configuration but LCP transmission. Our intention was to check for any systematic errors associated with such a change, although our understanding of the system is that there should be no such systematic errors. During acquisition of file 33605, we had to restart the data-acquisition system several times and noted diagonal lines across the real-time display, but we do not expect those problems to have affected the recorded data. Yet we are concerned that the SC/OC pattern in file 33605 does not match those in files 33603 and 33604. On the other hand, it is plausible that SC/OC for some portions of the surface might differ for LCP and RCP transmissions. Extensive dual-polarization imaging in 2000 and 2004 is needed to establish Toutatis' global SC/OC signature more thoroughly.

and the loss tangent is

$$\tan\delta = K_i/K_r. \quad (8)$$

Howell *et al.* (1994) find that Toutatis' S-class spectral signature appears to be consistent with the Gaffey *et al.* (1993) subclasses II, III, or IV, whose meteorite analogs include pallasites, L chondrites, H chondrites, and ureilites. Those rocks have diverse metal concentrations (and hence diverse electrical properties), and their solid-rock densities d range from about 3.5 g cm^{-3} for ordinary chondrites to 4.9 g cm^{-3} for stony irons (Ostro *et al.* 1991b and references therein). Ureilites contain no more than a few weight percent of free metal (Dodd 1981), so in this sense they compare with very metal-poor ordinary chondrites.

Campbell and Ulrichs (1969) measured the electrical properties of solid and powdered terrestrial rocks and meteorites, including two H chondrites and three L6 chondrites. They found 450-MHz values of $(K_r, \tan\delta)$ ranging from (8, 0.015) to (81, 0.19), that is, values of L from 4 to 0.1 wavelengths, for their solid meteorites. They did not report 35-GHz results for the meteorites, but they did find that values of L at 35 GHz mimic those at 450 MHz for their solid terrestrial samples.

The absorption lengths for unconsolidated particulate mixtures are longer than for solid rocks. Garvin *et al.* (1985) evaluated empirical relationships (e.g., Olhoeft and Strangway 1975) between radar-frequency values of K_r and bulk density $d_{\rm bulk} = (1 - p)d$ in units of g cm^{-3}, where p is porosity, for diverse naturally occurring terrestrial (metal-free) rocks and adopted:

$$K_r = 1.87^{d_{\rm bulk}} \quad (9)$$

Empirical relationships for $\tan\delta$ include the Olhoeft and Strangway (1975) equation:

$$\log_{10}(\tan\delta) = 0.440 d_{\rm bulk} - 2.943. \quad (10)$$

Estimates of the porosity of lunar soils (Carrier *et al.* 1973, Mitchell *et al.* 1974) range from 0.3 to 0.7, but nearly all fall between 0.35 and 0.55, in agreement with theoretical and empirical investigations of particle-packing phenomena (e.g., Gray 1968, Powell 1980). The average porosity for the top 30 cm of lunar soil is 0.49 (Heiken *et al.* 1991, Table 9.5). With that porosity and the typical solid-rock densities of ordinary chondrites and stony irons noted above, the above equations yield values of $(K_r, \tan\delta)$ ranging from (3, 0.0067) to (4.6, 0.014), that is, values of L from 14 to 5 wavelengths. However, metallic phases in concentrations seen in H chondrites and stony irons can produce loss tangents in powdered mixtures that are several times higher than those predicted by Eq. (10) (unpublished results of measurements performed by G. R. Olhoeft at USGS and W. Westphal of MIT on powdered mixtures of silica and stainless steel; see also Kelly *et al.* 1953), reducing L to two to three wavelengths.

These considerations suggest that our 3.5-cm echoes' penetration depth is no more than a few decimeters and possibly no more than a few centimeters. Additionally, Simpson (1976) showed that the effective penetration depth can be reduced dramatically if the subsurface density gradient matches the regolith's impedance to that of free space, or if it contains stratifications with lossy layers that create certain resonance effects. We conclude that multiple scattering from buried rocks probably does not make a significant contribution to Toutatis' echoes.

5.5. Surface Rocks

Single scattering from rocks on, or very near, the surface therefore is the leading candidate for the primary source of Toutatis' SC echo as well as an indeterminate, but possibly substantial, part of the OC echo. Infrared and optical data support the idea that Toutatis is moderately rough at "all" scales. Howell *et al.* (1994) modeled the thermal contribution to Toutatis' 3- to-3.5-μm flux and concluded that a rocky surface with some thermal inertia offered the best fits. The Hudson and Ostro (1998) analysis of optical lightcurves presented by Spencer *et al.* (1995) yielded a value of $32 \pm 8^\circ$ for Hapke's macroscopic roughness parameter $\bar{\theta}$, which is an integral property over all scales up to the resolution limit of the photometric data (Helfenstein 1988). In the HO95 analysis, structural scales up to $\sim$100 m are accounted for by the shape model itself, so the large value of $\bar{\theta}$ applies to several-decameter scales and below. Interpretation of Toutatis' OC scattering law (Section 5.3) in terms of the slope distribution of smooth facets (Mitchell *et al.* 1996) would imply rms slopes of $39 \pm 3^\circ$ within our unresolved, decameter-scale pixels, consistent with the $\bar{\theta}$ estimate. (Note, however, that the OC scattering law is a composite of effects from all contributors of OC echo. Since a diffuse component from rock echoes might have a lower value of n, that slope value might be an overestimate.)

Numerous studies have tried to relate the diffuse component of lunar and planetary radar echoes to near-surface rock populations (e.g., Pollack and Whitehill 1972, Calvin *et al.* 1988, Harmon and Ostro 1985). Baron *et al.* (1998) used estimates of Viking lander site rock populations to model the SC albedo due to single scattering from surface, partially buried, and completely buried rocks of various shapes. They compared their results to the equivalent full-disk SC albedo for the Viking lander sites (0.01 to 0.03; Harmon 1997) and concluded that surface rocks contribute more than buried rocks to diffuse echoes from areas surrounding the landing sites. Their modeling indicates that surface-rock backscattering laws can be complex, often peaking at oblique angles of incidence. This effect may help to explain the relative abundance of higher-$\mu_{\rm C}$ pixels near the trailing edges of the images in Fig. 4.

Toutatis' SC albedo, 0.07, is several times the values estimated for the Viking and Pathfinder lander sites (0.01 to 0.03; Harmon 1997), consistent with Toutatis having a greater surface coverage by rocks that are both rough and reflective.

Toutatis' μ_C is slightly lower than the value (about 0.4) for the diffuse component of the echo from the Mars lander sites, but this might be due to Toutatis' smooth-surface component having much steeper slopes than its counterpart on Mars, letting it contribute OC echo over a larger range of incidence angles.

A *first-order* estimate of the fraction C of Toutatis' surface that is covered by wavelength-and-larger rocks follows from the following simplifying assumptions:

(A) Multiple scattering is negligible and the echo is the sum of contributions from the smooth surface ($\mu_C = 0$) and rocks ($\mu_C = \mu_3$); this domain is at the bottom of the triangle in Fig. 3.

(B) Each component contributes power in proportion to its areal coverage and its radar reflectivity R.

(C) Rocks have solid-rock density d, porosity $p = 0$, and bulk density $d_{\rm bulk} = d$, whereas the smooth-surface component has porosity $p > 0$ and bulk density $d_{\rm bulk} = (1 - p)d$.

(D) Radar reflectivity R is related to bulk density $d_{\rm bulk}$ via the following empirical relation (Garvin *et al.* 1985):

$$R(d) = \{[1 - \exp(d_{\rm bulk}/3.2)]/[1 + \exp(d_{\rm bulk}/3.2)]\}^2. \quad (11)$$

(E) The radar albedo in any given polarization is the product of R and a backscatter gain factor g that contains effects of surface structure and target shape and orientation. [Whereas g would be unity for a smooth sphere, it would be slightly larger for a sphere whose surface is rough at virtually any scale(s) not much smaller than the wavelength. Toutatis' irregular shape makes g dependent on orientation, but we will work with the average disc-integrated properties in Table VIII, and we wish to average g over all observed orientations of the asteroid. A sphere with a $\cos^n\theta$ scattering law would have $g = (n + 2)/(n + 1)$. Our estimates of Toutatis' OC and SC scattering law exponents (Section 5.3) correspond to values of g within 0.05 of 1.27.]

Then the contribution to the OC albedo from the smooth surface is

$$\hat{\sigma}_{\rm OC,smooth} = (1 - C)gR[(1 - p)d]. \quad (12)$$

The contribution to the OC albedo from rocks is

$$\hat{\sigma}_{\rm OC,rocks} = CgR(d)/(1 + \mu_3). \quad (13)$$

The total OC albedo is

$$\hat{\sigma}_{\rm OC} = (1 - C)gR[(1 - p)d] + CgR(d)/(1 + \mu_3). \quad (14)$$

The entire SC albedo is from rocks, so

$$\hat{\sigma}_{\rm SC} = \hat{\sigma}_{\rm SC,rocks} = \mu_3 CgR(d)/(1 + \mu_3). \quad (15)$$

The net circular polarization ratio is

$$\mu_{\rm NET} = \frac{-C\mu_3 R(d)}{(-\mu_3 + C + C\mu_3 - 1)R[(1 - p)d] - R(d)C}. \quad (16)$$

Two expressions for rock coverage follow—one from Eq. (16),

$$C_1(\mu_3, \mu_{\rm NET}, d, p) = \frac{R[(1 - p)d]\mu_{\rm NET}(1 + \mu_3)}{R[(1 - p)d]\mu_{\rm NET}(1 + \mu_3) + R(d)(\mu_3 - \mu_{\rm NET})}, \quad (17)$$

and one from Eq. (15),

$$C_2(\mu_3, \mu_{\rm NET}, d, \hat{\sigma}_{\rm OC}, g) = \frac{\hat{\sigma}_{\rm OC}\mu_{\rm NET}(1 + \mu_3)}{R(d)g\mu_3}. \quad (18)$$

We stress that this admittedly simplistic approach is intended to provide first-order constraints on physical parameters. In this context, let us first examine the validity of applying Eq. (18) to the *diffuse component* of (13-cm) radar echoes from the Mars Viking Lander sites, for which we have estimates of $\hat{\sigma}_{\rm SC}$ that range from 0.0115 to 0.0316 (Harmon 1997; tabulated by Baron *et al.* 1998) as well as estimates of C that range from 0.14 to 0.188 (Moore *et al.* 1979, 1987; Moore and Jakosky 1989). Estimates of the scattering law exponent for Mars SC echoes typically range from about 1.0 (Harmon and Ostro 1985) to about 2.0 (Harmon *et al.* 1992), corresponding to values of g from 1.3 to 1.5. In keeping with the discussion in Section 5.1, let us assume that $\mu_3 = 0.5$. Then Eq. (18) predicts a rock density between 2.3 and 5.7 g cm^{-3}, an interval that encompasses the Christensen and Moore (1992) estimate, 2.6 g cm^{-3}, of the density of rocks at the Viking sites.

For Toutatis, we combine Eqs. (17) and (18) to estimate rock coverage and the smooth surface component's porosity for typical densities of ordinary chondrites (3.5 g cm^{-3}) and stony irons (4.9 g cm^{-3}), using $\mu_{\rm NET} = 0.29$ and $\mu_3 = 0.5$. Figure 5 plots C_1 and C_2 for $g = 1.27$ and $\hat{\sigma}_{\rm OC} = 0.21$, which is the OC albedo of a sphere with Toutatis' model scattering properties. The curves' intersection defines C and p for both solid-rock densities: $C = 58\%$ and $p = 21\%$ for $d = 3.5$ g cm^{-3}, and $C = 35\%$ and $p = 56\%$ for $d = 4.9$ g cm^{-3}. To demonstrate the sensitivity to those parameters, we list in Table IX the joint solutions for C and p for all four combinations of $g = 1.0$ and 1.3, and $\hat{\sigma}_{\rm OC} = 0.21$ and 0.24. Note that among these four combinations, the choice of $g = 1.3$ and $\hat{\sigma}_{\rm OC} = 0.21$ minimizes C and maximizes p.

Toutatis' average reflectivity, $R = 0.21/1.27 = 0.165$, is more than twice the Moon's value ($\sim$0.07 at wavelengths between 1 and 23 cm (Pettengill 1978)) and also more than the Venus's average value (0.13 at 17 cm), which Garvin *et al.* (1985) interpret to indicate a surface dominated by rocks and/or bedrock. Toutatis' high radar albedo naturally is easier to satisfy with high surface bulk density, but the modest polarization ratio restricts the coverage by rocks, whose $\mu_C = \mu_3 \cong 0.5$ is higher than Toutatis' value, $\mu_C = \mu_{\rm NET} = 0.29$; consequently a high bulk density can be achieved only by reducing the porosity of the smooth surface component. For $d = 3.5$ g cm^{-3}, our calculations lead to the conclusion that the smooth surface component cannot be porous. On the other hand, for $d = 4.9$ g cm^{-3}, a smooth-surface

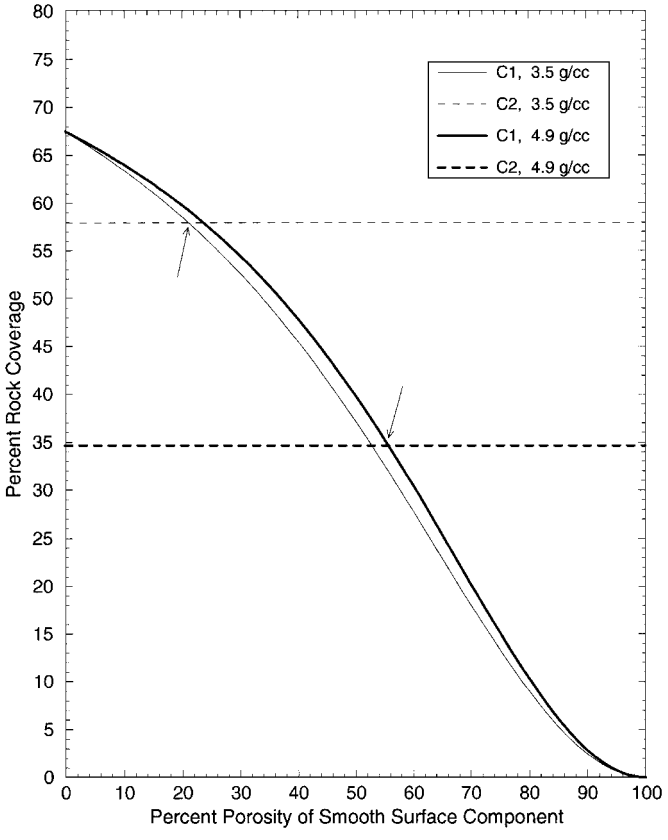

FIG. 5. Porosity and rock coverage for solid-rock density d equal to 3.5 g cm^{-3} (thin curves) and 4.9 g cm^{-3} (thick curves). For each value of d, the porosity (p) of Toutatis' smooth surface component is defined by the intersection (arrow) of the two expressions for rock coverage in the text: C_1 (solid curve) from Eq. (17) and C_2 (dashed curve) from Eq. (18). These curves, which used $\mu_{\rm NET} = 0.29$, $\mu_3 = 0.5$, $g = 1.27$, and $\hat{\sigma}_{\rm OC} = 0.21$, yield $C = 58\%$ and $p = 21\%$ for $d = 3.5$ g cm^{-3}, and $C = 35\%$ and $p = 56\%$ for $d = 4.9$ g cm^{-3}. Table IX gives results for other values of g and $\hat{\sigma}_{\rm OC}$.

component with porosity like that of lunar soil can satisfy the observations.

Therefore, if Toutatis is a stony–iron analog, then the smooth surface component probably is regolith that is at least several centimeters thick (see Section 5.4) and 1/3 covered by rocks. If Toutatis is an ordinary-chondrite analog, then the smooth surface component probably is essentially solid and at least half covered by rocks. For the smooth surface component to look solid to the radar, any overlying regolith probably cannot be much more than 1 cm thick. Of course, Toutatis' mineralogy is not necessarily represented in our meteorite sample, and solid-rock densities between (or beyond) the extreme values considered here are plausible. Nonetheless, for this asteroid, our results directly couple hypotheses about mineralogy to hypotheses about regolith generation and retention.

TABLE IX
Porosity and Rock Coverage

	$d = 3.5$ g cm^{-3}		$d = 4.9$ g cm^{-3}	
$\hat{\sigma}_{\rm OC}$	$g = 1.00$	$g = 1.27$	$g = 1.00$	$g = 1.27$
0.24	$C = 84\%$ $p < 0$	$C = 66\%$ $p = 3\%$	$C = 50\%$ $p = 37\%$	$C = 40\%$ $p = 50\%$
0.21	$C = 74\%$ $p < 0$	$C = 58\%$ $p = 21\%$	$C = 44\%$ $p = 45\%$	$C = 35\%$ $p = 56\%$

Note. Estimates of the porosity, p, of Toutatis' smooth surface component and the rock coverage C are defined by Eqs. (17) and (18) for the listed values of solid-rock density d and backscatter gain g. Where "$p < 0$" is written, equating Eqs. (17) and (18) with the indicated parameters yields a (nonphysical) negative porosity.

ACKNOWLEDGMENTS

Part of this research was conducted at the Jet Propulsion Laboratory, California Institute of Technology, under contract with the National Aeronautics and Space Administration (NASA). Work at Washington State University was supported in part by NASA Grant NAGW-4636.

REFERENCES

Baron, J. E., R. A. Simpson, G. L. Tyler, H. J. Moore, and J. K. Harmon 1998. Estimation of Mars radar backscatter from measured surface rock populations. *J. Geophys. Res.* **103**, 22695–22712.

Calvin, W. M., B. M. Jakosky, and P. R. Christensen 1988. A model of diffuse radar scattering from martian surface rocks. *Icarus* **76**, 513–524.

Campbell, M. J., and J. Ulrichs 1969. Electrical properties of rocks and their significance for lunar radar observations. *J. Geophys. Res.* **74**, 5867–5880.

Carrier, W. D., III, J. K. Mitchell, and A. Mahmood 1973. The relative density of lunar soil. *Proc. Lunar Sci. Conf.* **4**, 2403–2411.

Chandrasekhar, S. 1960. *Radiative Transfer.* Dover, New York.

Christensen, P. R., and H. J. Moore 1992. The martian surface layer. In *Mars* (H. H. Keiffer, B. M. Jakosky, C. W. Snyder, and M. S. Matthews, Eds.), pp. 686–729. Univ. of Arizona Press, Tucson.

Cuzzi, J. N., and J. B. Pollack 1978. Saturn's rings: Particle composition and size distribution as constrained by microwave observations. I. Radar observations. *Icarus* **33**, 23–262.

Dodd, R. T. 1981. *Meteorites*, Chap. 9. Cambridge Univ. Press, New York.

Finney, D. J. 1964. *Statistical Methods in Biological Assay*, 2nd ed., p. 24. Hafner, New York.

Gaffey, M. J., J. F. Bell, R. H. Brown, T. H. Burbine, J. L. Piatek, K. L. Reed, and D. A. Chaky 1993. Mineralogical variations within the S-type asteroid class. *Icarus* **106**, 573–602.

Garvin, J. B., J. W. Head, G. H. Pettengill, and S. H. Zisk 1985. Venus global radar reflectivity and correlations with elevation. *J. Geophys. Res.* **90**, 6859–6871.

Gray, W. A. 1968. *The Packing of Solid Particles*, pp. 43–107. Chapman and Hall, London.

Guenther, R. D. 1990. *Modern Optics*. Wiley, New York.

Haldemann, A. F. C., D. O. Muhleman, B. Butler, and M. A. Slade 1997. The western hemisphere of Venus: 3.5 cm dual circular-polarization radar images. *Icarus* **128**, 398–414.

Hapke, B. 1993. *Theory of Reflectance and Emittance Spectroscopy*. Cambridge Univ. Press, New York.

Harmon, J. K. 1997. A radar study of the Chryse region, Mars. *J. Geophys. Res.* **102**, 4081–4095.

Harmon, J. K., and S. J. Ostro 1985. Mars: Dual-polarization radar observations with extended coverage. *Icarus* **62**, 110–128.

Harmon, J. K., M. A. Slade, and R. S. Hudson 1992. Mars radar scattering: Arecibo/Goldstone results at 12.6- and 3.5-cm wavelengths. *Icarus* **98**, 240–253.

Heiken, G. H., D. T. Vaniman, and B. M. French 1991. *Lunar Sourcebook.* Cambridge Univ. Press, New York.

Helfenstein, P. 1988. The geological interpretation of photometric surface roughness. *Icarus* **73**, 462–481.

Howell, E. S., D. T. Britt, J. F. Bell, R. P. Binzel, and L. A. Lebofsky 1994. Visible and near-infrared spectral observations of 4179 Toutatis. *Icarus* **111**, 468–474.

Hudson, R. S., and S. J. Ostro 1995. Shape and non-principal axis spin state of asteroid 4179 Toutatis. *Science* **270**, 84–86.

Hudson, R. S., and S. J. Ostro 1996. Asteroid 4179 Toutatis: Potential of 1996 radar observations for spin-state refinement. *Bull. Am. Astron. Soc.* **28**, 1105.

Hudson, R. S., and S. J. Ostro 1998. Photometric properties of asteroid 4179 Toutatis from lightcurves and a radar-derived physical model. *Icarus* **135**, 451–457.

Kelly, J. M., J. O. Stenoien, and D. E. Isbell 1953. Wave-guide measurements in the microwave region on metal powders suspended in paraffin wax. *J. Appl. Physics* **24**, 258–262.

Lazzarin, M., C. Barbieri, and F. Marzari 1994. CCD reflectance spectra of Apollo asteroid 4179 Toutatis. *Planet. Space Sci.* **42**, 327–336.

Liou, K., and R. M. Schotland 1971. Multiple backscattering from water clouds for a pulsed lidar system. *J. Atmos. Sci.* **22**, 772–784.

Long, M. W. 1965. On the polarization and wavelength dependence of sea echo. *Trans. IEEE* **AP-14**, 749–754.

Lupishko, D. F., S. V. Vasilyev, Ju. S. Efimov, and N. M. Shakhofskoj 1995. UBVRI-polarimetry of asteroid 4179 Toutatis. *Icarus* **113**, 200–205.

Marsden, B. G. 1970. On the relationship between comets and minor planets. *Astron. J.* **75**, 206–217.

Marsden, B. G. 1989a. 1989 AC. *IAU Circ.* 4701.

Marsden, B. G. 1989b. (4179)* 1989 AC = 1934 CT. *Minor Planet Circ.* 15061.

Marsden, B. G. 1989c. 1989 AC. *IAU Circ.* 4715.

Marsden, B. G. 1990. (4179) Toutatis = 1989 AC. *Minor Planet Circ.* 16444.

McNeil, W. R., and A. I. Carswell 1975. Lidar polarization studies of the troposphere. *Appl. Opt.* **14**, 2158–2168.

Milani, A., M. Carpino, G. Hahn, and A. M. Nobili 1989. Dynamics of planet-crossing asteroids: Classes of orbital behavior. *Icarus* **78**, 212–269.

Mitchell, J. K., W. N. Houston, W. D. Carrier, III, and N. C. Costes 1974. *Apollo Soil Mechanics Experiment S-200*, Final Report, NASA Contract NAS 9-11266, Space Science Laboratory Series 15, Issue 7. Univ. of California, Berkeley.

Mitchell, D. L., S. J. Ostro, R. S. Hudson, K. D. Rosema, D. B. Campbell, R. Velez, J. F. Chandler, I. I. Shapiro, J. D. Giorgini, and D. K. Yeomans 1996. Radar observations of asteroids 1 Ceres, 2 Pallas, and 4 Vesta. *Icarus* **124**, 113–133.

Moore, H. J., and B. M. Jakosky 1989. Viking landing sites, remote sensing observations, and physical properties of martian surface materials. *Icarus* **81**, 164–184.

Moore, H. J., C. R. Spitzer, K. Z. Bradford, P. M. Cates, R. E. Hutton, and R. W. Shorthill 1979. Sample fields of the Viking landers, physical properties, and aeolian processes. *J. Geophys. Res.* **84**, 8365–8377.

Moore, H. J., R. E. Hutton, G. D. Clow, and C. R. Spitzer 1987. Physical properties of the surface materials of the Viking landing sites on Mars. *U. S. Geol. Survey Prof. Pap.* **1389**.

Muinonen, K. 1996. Orbital covariance eigenproblem for asteroids and comets. *Mon. Not. R. Astron. Soc.* **280**, 1235–1238.

Muinonen, K. 1998. Discovery and follow-up simulations for small Earth-crossing asteroids. *Planet. Space Sci.* **46**, 291–297.

Mukai, T., T. Iwata, S. Kikuchi, R. Hirata, M. Matsumura, Y. Nakamura, S. Narusawa, A. Okazaki, M. Seki, and K. Hayashi 1997. Polarimetric observations of 4179 Toutatis in 1992/1993. *Icarus* **127**, 452–460.

Olhoeft, G. R., and D. W. Strangway 1975. Dielectric properties of the first 100 meters of the Moon. *Earth Planet. Sci. Lett.* **24**, 394–404.

Ostro, S. J. 1993. Planetary radar astronomy. *Rev. Mod. Phys.* **65**, 1235–1279.

Ostro, S. J., D. B. Campbell, J. F. Chandler, I. I. Shapiro, A. A. Hine, R. Velez, R. F. Jurgens, K. D. Rosema, R. Winkler, and D. K. Yeomans 1991a. Asteroid radar astrometry. *Astron. J.* **102**, 1490–1502.

Ostro, S. J., D. B. Campbell, J. F. Chandler, A. A. Hine, R. S. Hudson, K. D. Rosema, and I. I. Shapiro 1991b. Asteroid 1986 DA: Radar evidence for a metallic composition. *Science* **252**, 1399–1404.

Ostro, S. J., R. S. Hudson, R. F. Jurgens, K. D. Rosema, R. Winkler, D. Howard, R. Rose, M. A. Slade, D. K. Yeomans, J. D. Giorgini, D. B. Campbell, P. Perillat, J. F. Chandler, and I. I. Shapiro 1995. Radar images of asteroid 4179 Toutatis. *Science* **270**, 80–83.

Ostro, S. J., R. F. Jurgens, K. D. Rosema, R. S. Hudson, J. D. Giorgini, R. Winkler, D. K. Yeomans, D. Choate, R. Rose, M. A. Slade, S. D. Howard, D. J. Scheeres, and D. L. Mitchell 1996. Radar observations of asteroid 1620 Geographos. *Icarus* **121**, 44–66.

Pal, S. R., and A. I. Carswell 1977. The polarization characteristics of lidar scattering from snow and ice crystals in the atmosphere. *J. Appl. Meteorol.* **16**, 70–80.

Pettengill, G. H. 1978. Physical properties of the planets and satellites from radar observations. *Ann. Rev. Astron. Astrophys.* **16**, 265–292.

Pollack, J. B., and L. Whitehill 1972. A multiple-scattering model of the diffuse component of lunar radar echoes. *J. Geophys. Res.* **77**, 4289–4303.

Powell, M. J. 1980. Computer-simulated random packing of spheres. *Powder Technol.* **25**, 45–52.

Priest, P. 1993. *Goldstone Solar System Radar Capability and Performance*, Internal Report 1740-4. Jet Propulsion Laboratory, Pasadena, CA.

Sassen, K. 1974. Depolarization of laser light backscattered by artificial clouds. *J. Atmos. Sci.* **13**, 923.

Sassen, K. 1975. Laser depolarization "bright band" from melting snowflakes. *Nature* **255**, 316–318.

Schotland, R. M., K. Sassen, and R. Stone 1971. Observations by lidar of linear depolarization ratios for hydrometeors. *J. Appl. Meteorol.* **10**, 1011–1017.

Simpson, R. A. 1976. Electromagnetic reflection and transmission at interfaces involving graded dielectrics with applications to planetary radar astronomy. *IEEE Trans. Antenna Propag.* **AP-24**, 17–24.

Spencer, J. R., L. A. Akimov, C. Angeli, P. Angelini, M. A. Barucci, P. Birch, C. Blanco, M. W. Buie, A. Caruso, V. G. Chiornij, F. Colas, P. Dentchev, N. I. Dorokhov, M. Cristina De Sanctis, E. Dotto, O. B. Ezhkova, M. Fulchignoni, S. Green, A. W. Harris, E. S. Howell, T. Hudecek, A. V. Kalashnikov, V. V. Kobelev, Z. B. Korobova, N. I. Koshkin, V. P. Kozhevnikov, Y. N. Krugly, D. Lazzaro, J. Lecacheux, J. MacConnell, S. Y. Mel'nikov, T. Michalowski, B. E. A. Mueller, T. Nakamura, C. Neese, M. C. Nolan, W. Osborn, P. Pravec, D. Riccioli, V. S. Shevchenko, V. G. Shevchenko, D. J. Tholen, F. P. Velichko, R. Venditti, W. Wisniewski, J. Young, and B. Zellner 1995. The lightcurve of 4179 Toutatis: Evidence for complex rotation. *Icarus* **117**, 71–89.

Stacy, N. J. S. 1993. *High-resolution synthetic aperture radar observations of the Moon.* Ph.D. thesis, Cornell Univ.

Stacy, N. J. S., D. B. Campbell, and P. G. Ford 1997. Arecibo radar mapping of the lunar poles: A search for ice deposits. *Science* **276**, 1527–1530.

Tholen, D. J., and J. R. Spencer 1992. Close encounters of the asteroidal kind: A preview of upcoming encounters with 243 Ida and 4179 Toutatis. *Bull. Am. Astron. Soc.* **24**, 934.

Thompson, T. W., S. H. Zisk, R. W. Shorthill, and J. A. Cutts 1981. Lunar craters with radar bright ejecta. *Icarus* **46**, 201–225.

Veverka, J., P. Thomas, A. Harch, B. Clark, J. F. Bell III, B. Carcich, J. Joseph, C. Chapman, W. Merline, M. Robinson, M. Malin, L. A. McFadden, S. Murchie, S. E. Hawkins III, R. Farquhar, N. Izenberg, and A. Cheng 1997. NEAR's flyby of 253 Mathilde: Images of a C asteroid. *Science* **278**, 2109–2114.

Whipple, A. L. 1995. Lyapunov times of the inner asteroids. *Icarus* **115**, 347–353.

Whipple, A. L., and P. J. Shelus 1993. Long-term dynamical evolution of the minor planet (4179) Toutatis. *Icarus* **105**, 408–419.

Yeomans, D. K., and P. W. Chodas 1994. Predicting close approaches of asteroids and comets to Earth. In *Hazards Due to Comets and Asteroids* (T. Gehrels, Ed.), pp. 241–258. Univ. of Arizona Press, Tucson.

Zaitsev, A. L., A. G. Sokolsky, O. R. Rzhiga, A. S. Vyshlov, A. P. Krivtsov, and V. A. Shubin 1993. Radar investigation of asteroid 4179 Toutatis with 6 cm waves. *Radiotekhnika Elektronika* **38**, 1842–1850. [in Russian; translation: Zaytsev, A. L., A. G. Sokol'skiy, O. R. Rzhiga, A. S. Vyshlov, A. P. Krivtsov, and V. A. Shubin 1993. Radar investigations of the asteroid 4179 Tautatis at wavelength of 6 cm. *J. Comm. Tech. Electronics* **38:16**, 135–143 [in English, by Scripta Technica, Inc., 1994]]